

論文 / 著書情報
Article / Book Information

Title	Signatures of a Nonthermal Metastable State in Copropagating Quantum Hall Edge Channels
Authors	Toshimasa Fujisawa, Kosuke Itoh, Ryo Nakazawa, Tomoaki Ota, Masayuki Hashisaka, Koji Muraki
Citation	Physical Review Letters, Vol. 120, 19, 197701
Pub. date	2018, 5
Pub. version	https://doi.org/10.1103/PhysRevLett.120.197701
Copyright	(C) 2018 American Physical Society

Signatures of a non-thermal metastable state in copropagating quantum Hall edge channels

Kosuke Itoh,¹ Ryo Nakazawa,¹ Tomoaki Ota,¹ Masayuki Hashisaka,^{1,2} Koji Muraki,² and Toshimasa Fujisawa^{1,*}

¹*Department of Physics, Tokyo Institute of Technology,
2-12-1 Ookayama, Meguro, Tokyo, 152-8551, Japan.*

²*NTT Basic Research Laboratories, NTT Corporation,
3-1 Morinosato-Wakamiya, Atsugi, 243-0198, Japan.*

(Dated: April 7, 2018)

A Tomonaga-Luttinger (TL) liquid is known as an integrable system, in which a non-equilibrium many-body state survives without relaxing to a thermalized state. This intriguing characteristic is tested experimentally in copropagating quantum Hall edge channels at bulk filling factor $\nu = 2$. The unidirectional transport allows us to investigate the time evolution by measuring the spatial evolution of the electronic states. The initial state is prepared with a biased quantum point contact, and its spatial evolution is measured with a quantum-dot energy spectrometer. We find strong evidences for a non-thermal metastable state in agreement with the TL theory before the system relaxes to thermal equilibrium with coupling to the environment.

Electron-electron interaction in usual conductors is often considered to bring the system in a thermalized state irrespective of the initial states [1–3]. In the case of one-dimensional Tomonaga-Luttinger (TL) liquids with interacting electrons, the integrable TL model suggests the presence of many conserved quantities and the absence of thermalization processes [4–6]. In the presence of weak non-integrable interactions, the system exhibits two-stage equilibration from an initial non-equilibrium state through an intermediate non-thermal metastable state to a thermalized state [7, 8]. While such intriguing dynamics have been observed in ultracold atoms [9, 10], solid-state realization would open vast non-equilibrium many-body physics particularly for transporting massive information. Edge channels in the integer quantum Hall regime can host a chiral TL liquid particularly at bulk Landau filling factor $\nu = 2$ with spin-up and -down edge channels [11, 12]. Electrons in the channels are mutually interacting, and collective excitation (plasmon) modes appear as the charge and spin (or dipole) modes, which have symmetric and anti-symmetric charge distribution, respectively, for the two channels if drift velocity difference is negligible [13]. This spin-charge separation has been identified in various measurements such as time- and spin-resolved measurement [14, 15], frequency-domain plasmon interference [16], and shot-noise detection [17]. A promising scheme for studying the equilibration dynamics is quantum dot (QD) energy spectroscopy for a non-equilibrium state prepared by a biased quantum point contact (QPC) [8, 18], where non-thermal states can be identified by observing non-Fermi distribution functions. Although the previous work [19] was successful in observing a spectral change, the non-thermal metastable state was not resolved as the resulting spectrum looked like a Fermi distribution function. As this can be explained by either the TL model [20] or

a stochastic scattering model [21], conclusive evidence is highly desirable.

In this work, we used the same QD-QPC scheme but investigated systematically to see how the energy distribution function changes with the initial state and the traveling distance. The expected non-thermal metastable state is successfully identified with an arctangent distribution function by setting the QPC at a low tunneling probability. The spectral change in the first equilibration is consistent with the plasmon excitations based on the TL model. The second equilibration toward cold Fermi distribution suggests weak coupling to the environment. In this way, the edge channels provide a unique opportunity for studying the integrability in a solid state system.

Figure 1(a) shows a schematic measurement setup for investigating copropagating edge channels, C_{\uparrow} for spin up and C_{\downarrow} for spin down, along a side of a two-dimensional electron system (2DES) at $\nu = 2$ under a perpendicular magnetic field B . The two ohmic contacts on both ends are always grounded at base temperature T_{base} . Non-equilibrium charge is injected from similar $\nu = 2$ edge channels, shown in the lower left, with bias voltage V_S through a QPC at conductance $(e^2/h)D$. Here, channel C_{\uparrow} can be excited by spin-up tunneling at $0 < D < 1$, and C_{\downarrow} by spin-down tunneling at $1 < D < 2$. The charge flows to the downstream, and the electronic state at the distance L from the QPC is investigated by a QD spectrometer with an energy level ε that can be tuned with the QD gate voltage V_{QD} . With appropriate bias voltage V_D on similar $\nu = 2$ edge channels in the lower right, the current $I_D(\varepsilon)$ through the dot level can be made proportional to the energy distribution function $f_{\uparrow}(\varepsilon)$ in channel C_{\uparrow} as described below.

The initial energy distribution function in C_{\uparrow} is expected to be a double-step function with height D and width eV_S by assuming energy-independent tunneling probability, as shown in panel (i) for $D = 0.5$ and (ii) for $D = 0.01$ of Fig. 1(b). For $D < 1$, one may consider that single electrons are randomly injected

* fujisawa@phys.titech.ac.jp

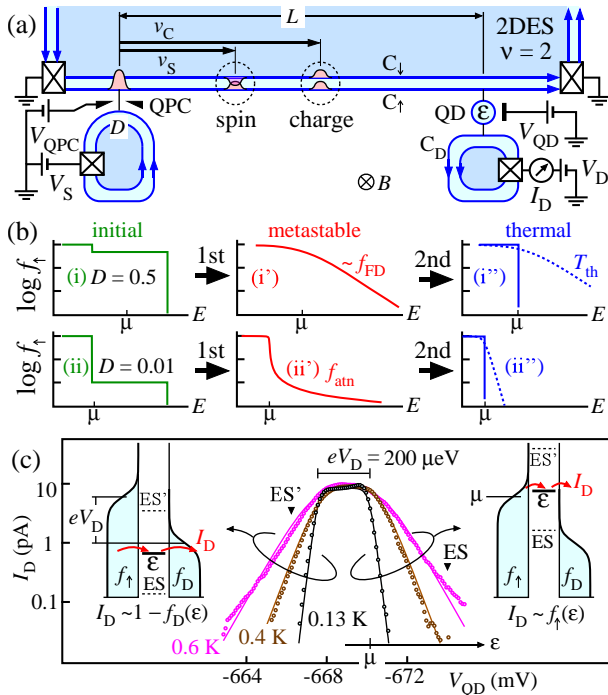


FIG. 1. (a) Schematic setup for the energy spectroscopy on copropagating channels C_\uparrow and C_\downarrow . (b) Expected two-stage equilibration from initial states with double-step distribution function in panel (i) at $D = 0.5$ and (ii) at $D = 0.01$, through metastable states in (i') and (ii'), to thermalized states in (i'') and (ii'') with dashed lines for a closed system and solid lines for an open system. (c) Current profiles of the QD spectrometer at various lattice temperatures. The energy diagrams in the left and right insets show that the currents on the left and right sides are proportional to the distribution functions $1 - f_D$ and f_\uparrow , respectively. Current through ES (ES') is allowed only when the ground state at ϵ is occupied (empty).

to C_\uparrow at a rate of $(e/h)DV_S$. The uncertainty relation implies that each electron wavepacket has a spread h/eV_S in time, and vh/eV_S in space for velocity v in the channel. The coupling between C_\uparrow and C_\downarrow splits each wavepacket into charge and spin wavepackets as illustrated in Fig. 1(a) [15]. The length required for the spin-charge separation is given by $\ell_{SC} = hv_{SC}/eV_S$ with the relative velocity $v_{SC} = v_C v_S / (v_C - v_S)$ for charge and spin velocities v_C and v_S , respectively. Levkivskiy and Sukhorukov have calculated the energy distribution function at large distances beyond the spin-charge separation length ℓ_{SC} [8]. It is close to, but should be slightly different from, the Fermi distribution function $f_{FD}(E) = [1 + e^{(E-\mu)/k_B T_{th}}]^{-1}$ at thermalization temperature $T_{th} = \sqrt{\frac{3}{2}} \frac{1}{\pi k_B} \sqrt{D(1-D)} eV_S$ when the tunneling is frequent at $D \simeq 0.5$ [panel (i') in Fig. 1(b) for $D = 0.5$]. Here, μ is the corresponding chemical potential. In contrast, when the tunneling events are sparse ($D \ll 1$), a non-thermal metastable state with a non-trivial distribution function of an arctangent form

$f_{atn}(E) = \frac{1}{2} - \arctan(E/\Gamma)/\pi$ (a Lorentzian function in df/dE [8]) is expected to emerge with $\Gamma = 2eDV_S/\pi$ [panel (ii') for $D = 0.01$]. Intriguingly, no scattering happens even when a fast charge wavepacket overtakes a slow spin wavepacket, and thus there should be no further thermalization processes in the integrable model. Actual devices may have other thermalization processes. If the thermalization is associated with the non-integrable interaction within the channel, the system may relax to a heat-conserved thermalized state with a Fermi distribution function at T_{th} [the dashed lines in panels (i'') and (ii'')] after a long travel. If the system is weakly coupled to the environment, the system relaxes to a thermalized state at T_{base} (the solid lines). We shall investigate such two-stage equilibration.

We used a couple of devices with different length L ranging from 0.12 to 15 μm between the QD and QPC (See Appendix A). They are fabricated in standard AlGaAs/GaAs heterostructures with the electron density of 2.9 and $3.1 \times 10^{11} \text{ cm}^{-2}$ and low-temperature mobility of 1.6 and $1.9 \times 10^6 \text{ cm}^2/\text{Vs}$, and measured at $B = 6$ and 7.5 T, respectively for $L \geq 5$ and $L \leq 0.5 \mu\text{m}$ devices in a dilution refrigerator at $T_{base} = 80 - 110 \text{ mK}$. Finite current in I_D is observed when the energy level ϵ of the ground state is located in the transport window of the width eV_D (typically 200 μeV), as shown in Fig. 1(c). The temperature dependence shows a clear heating effect in both sides of the peak. All traces are fitted nicely with the Fermi distribution function over more than two orders of magnitude. As shown in the insets, I_D is proportional to f_\uparrow on the right side, where we focus in the following measurements, and to $(1 - f_D)$ with distribution function f_D in the drain channel C_D on the left side. In practice, excited states in the QD may contribute additional current (See Appendix B). The downward triangles labeled ES and ES' in all plots represent the conditions of excited states being aligned to one of the chemical potentials in the channels. Data in Fig. 1(c) shows that the excited states play a minor role when the channels show Fermi distribution functions.

Now, we investigate non-equilibrium states with the QPC. First, we focus on the first equilibration occurring at $L \sim \ell_{SC}$. Since ℓ_{SC} is tunable with V_S , the first equilibration can be studied with varying L and ℓ_{SC} . Here, ℓ_{SC} is estimated by using $v_{SC} = 27 \text{ km/s}$ obtained in the following analysis. As summarized in Figs. 2(a) and 2(b), the double-step current profile is clearly resolved in trace (i) taken at $L = 0.12 \mu\text{m} \ll \ell_{SC} = 1.1 \mu\text{m}$ ($V_S = 100 \mu\text{V}$), but gradually smeared out as seen in trace (ii) at $L = 0.5 \mu\text{m} < \ell_{SC} = 1.1 \mu\text{m}$ and (iii) at $L = 0.5 \mu\text{m} \sim \ell_{SC} = 0.7 \mu\text{m}$ ($V_S = 150 \mu\text{V}$). Their step positions were determined from the peak positions in the derivative (lower traces). The distance between the two steps, Δ evaluated in energy, deviates from the original step width eV_S with increasing L and V_S .

Figure 2(c) summarizes the normalized step width Δ/eV_S as a function of the interaction strength defined by $u \equiv e|V_S|L/h$. Data points taken at various L , V_S , and

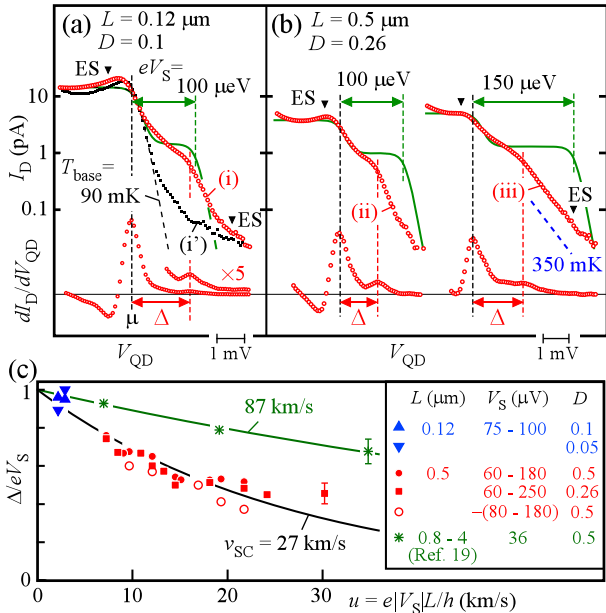


FIG. 2. (a) and (b) QD current profiles and their derivatives on the right side of the current peak. The double-step feature is clear in (i), but smeared out with reduced step distance Δ in (ii) at longer L and in (iii) at larger V_S . The reference trace (i') for the background excitation level is taken under opposite chirality. The black dashed curve in (a) shows f_{FD} at $T_{\text{base}} = 90 \text{ mK}$. The green solid lines show the initial double-step function at T_{base} . (c) The normalized step distance Δ/eV_S as a function of $u \equiv e|V_S|L/h$. The solid lines are exponential fits to our data with $v_{\text{SC}} = 27 \text{ km/s}$ and the data in ref. [19] with 87 km/s .

D follow single monotonic functions (solid lines). As we are not aware of theoretical formula for this dependence, an exponential dependence $\Delta/eV_S = \exp(-L/\ell_{\text{SC}}) = \exp(-u/v_{\text{SC}})$ is assumed for the solid lines with $v_{\text{SC}} = 27 \text{ km/s}$ for our devices and 87 km/s for the devices in Ref. [19] with an additional surface gate. These values are close to $v_{\text{SC}} = 60 - 75 \text{ km/s}$ obtained from a time-of-flight experiment in Ref. [15]. The variation may stem from the different geometries of the metal gate that partially screens the interaction [22–24]. Note that the observed V_S dependence in Fig. 2(c) does not agree with the *stochastic* electron-electron scattering approach [25], where the energy loss ($eV_S - \Delta$) is found to be independent of V_S . Our systematic study supports that the first-stage equilibration is associated with the *deterministic* spin-charge separation.

Let us investigate the energy distribution function at $L > \ell_{\text{SC}}$. Figure 3(a) shows the current profile taken at $L = 5 \mu\text{m}$ and $D = 0.005$, where unusual distribution functions with a long tail appear. We find excellent agreement with the theoretically predicted arctangent function (the red solid lines), where the single parameter $\Gamma = 2hI_S/\pi e$ was determined from the measurement of I_S . As ℓ_{SC} decreases with increasing V_S , no significant

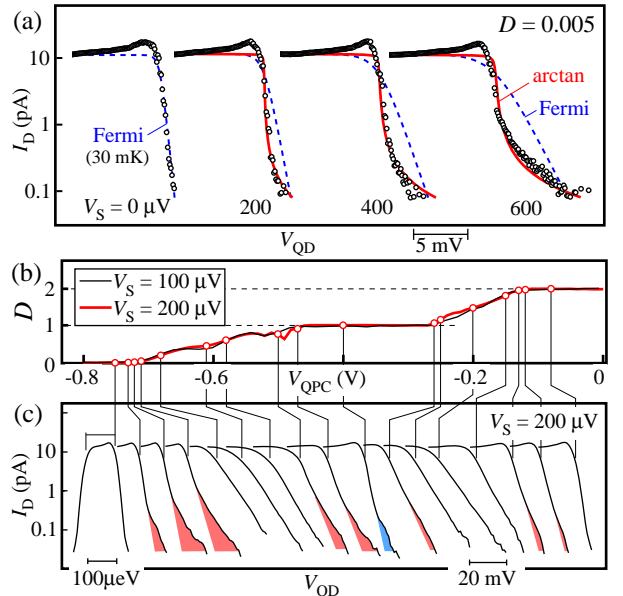


FIG. 3. (a) V_S dependence of the QD current profile obtained at small $D = 0.005$, showing an excellent agreement with the arctangent function (the red solid lines). No features approaching to the Fermi distribution function (the blue dashed lines for T_{th}) are seen. A peak near the Fermi edge is associated with the Fermi edge singularity (See Appendix A3). (b) Gate voltage V_{QPC} dependence of dimensionless conductance D of the QPC, where the series resistance in the setup was subtracted. (c) QD current profiles at various D marked by open circles in (b). Non-thermal current tail in (c) is highlighted by red and blue regions. The small tail in the blue region for $D = 1$ might be induced by spin-flip tunneling between the channels. Each profile in (a) and (c) is offset horizontally for clarity. The width of the current peak at $D = 0$ corresponds $eV_D = 200 \mu\text{eV}$ in (a) and $100 \mu\text{eV}$ in (c).

departure from the arctangent from is seen even at the longest relative distance L/ℓ_{SC} reaching 28 at $V_S = 600 \mu\text{V}$ ($\ell_{\text{SC}} = 0.18 \mu\text{m}$).

To identify the region where the non-thermal state emerges, the QD current spectra in Fig. 3(c) are taken at various D ranging from 0 to 2 marked by red circles in the QPC conductance steps of Fig. 3(b). While nearly Fermi distribution [showing a straight line in the low-current region of Fig. 3(c)] appears under frequent-tunneling conditions $D \simeq 0.5$ and $D \simeq 1.5$, non-Fermi distribution with a tail (marked by red regions) are observed under sparse-tunneling conditions $0 < D < 0.3$, $0.7 < D < 1.3$, and $1.7 < D < 2$. Quantitatively similar behavior is observed for the spin-up ($0 < D < 1$) and spin-down ($1 < D < 2$) tunneling, consistent with the interpretation that the energy exchange occurs via spin-charge separation. Detailed analysis on this data is shown in Appendix C.

If the current tail is associated with the non-thermal state of the TL model, it should be stable for long traveling before the second equilibration comes in. As shown

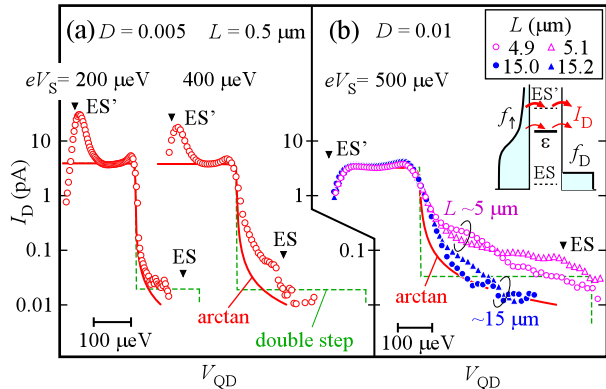


FIG. 4. (a) QD current profiles at $L \simeq 0.5 \mu\text{m}$. (b) QD current profiles at $L \simeq 5$ and $15 \mu\text{m}$. The unusual current tail is observed all traces. The tail is larger than expected (the solid line for the arctangent function) due to the excess current through ES' as shown in the inset. The dashed lines show the double-step function at $T_{\text{base}} = 0$. The inset shows the energy diagram for QD spectroscopy with excited states, ES and ES' .

in Fig. 4(a), non-thermal states showing non-exponential current tails are well developed at $L = 0.5 \mu\text{m}$ close to $\ell_{\text{SC}} = 0.55 \mu\text{m}$ ($V_{\text{S}} = 200 \mu\text{V}$) and greater than $\ell_{\text{SC}} = 0.28 \mu\text{m}$ ($V_{\text{S}} = 400 \mu\text{V}$). Similar current profiles are also seen at much longer distances $L \simeq 5$ and $15 \mu\text{m}$ as compared to $\ell_{\text{SC}} = 0.22 \mu\text{m}$ ($V_{\text{S}} = 500 \mu\text{V}$) in Fig. 4(b). Although they were measured at slightly different conditions with different samples, quite similar current profiles showing a long tail are reproduced in the wide range of L . This manifests the long-lived nature of the non-thermal state.

The data in Fig. 4(b) were measured using the same QD spectrometer while the excitation being done with different QPCs. Although the QPC characteristics are slightly different, the long tail of the distribution function seems to be attenuated as L increases from 5 to 15 μm . Similar attenuation with the decay length of about $\ell_{\text{leak}} = 20 \mu\text{m}$ is also seen at $D = 0.5$ and $V_{\text{S}} = 200 \mu\text{V}$ (See Appendix C3). This suggests heat leakage to the environment. Although we need further studies to identify its origin, it could be related to spin-flip tunneling between the channels [26, 27], plasmon scattering with counterpropagating channels [22, 28, 29], excitation in remote channels [30], and coupling to phonons [31, 32].

In this way, the expected non-thermal metastable state is clearly demonstrated. The evidence is reinforced by the following arguments excluding experimental artifacts.

We performed similar experiments at the reversed magnetic field where, due to opposite chirality, plasmon excitations cannot reach the QD detector. We observed no measurable influence on I_{D} at $L \geq 0.5 \mu\text{m}$. A small excess current for the shortest distance of $L = 0.12 \mu\text{m}$ [trace (i') at $B = -7.5 \text{ T}$ in Fig. 2(a)] is possibly due to photon assisted tunneling via electrostatic coupling be-

tween the QPC and the QD [33]. This ensures that the current tail observed at $B > 0$ is associated with the chiral plasmons in the edge channel.

Spin-flip tunneling between C_{\uparrow} and C_{\downarrow} can influence the distribution function. This effect should be maximized at $D = 1$, where we observed in a separate measurement with the same sample that about 0.5 % of injected electrons in C_{\uparrow} experience tunneling to C_{\downarrow} during the propagation of $15 \mu\text{m}$ at $V_{\text{S}} = 200 \mu\text{V}$ [26, 27]. This unwanted excitation might be the reason for having a small current tail (the blue region) at $D = 1$ in Fig. 3(c). The spin-flip tunneling should play a minor role at $D \ll 1$.

The QPCs used in this work show nonlinear current-voltage characteristics [34] (See Appendix A2). The QPC used for Fig. 3 shows reasonable linearity up to $200 \mu\text{V}$, where the data in Fig. 3(c) was taken, as shown by the small difference between the QPC conductance steps at $V_{\text{S}} = 100$ and $200 \mu\text{V}$ in Fig. 3(b). The linearity holds even up to $V_{\text{S}} \simeq 500 \mu\text{V}$ for small $D = 0.005$, where the clear arctangent profile in Fig. 3(a) is obtained. Therefore, the nonlinearity should play a minor role in the appearance of non-thermal states. However, the nonlinearity can deflect or increase the distribution function from the expected arctangent form, which could be the case for the data of Fig. 4.

While the calculated current profiles presented here were obtained by solving rate equations with the ground state of the QD only, we also checked the effects of excited states [35] (See Appendix B). For Fermi distribution functions, the inclusion of the excited states in the simulation did not change the current profile significantly. In contrast, for arctangent functions, the current profile changed considerably when the excited states have larger tunneling rates than the ground state. This also explains why the observed current in Fig. 4 is greater than the calculated one with the ground state only. We note that in Fig. 3 the measured current in the tail agrees well with the calculation, where this QD shows small tunneling rates for the excited states (See Appendix A3).

In summary, we have successfully observed non-thermal states with arctangent energy distribution functions. This suggests that the system can be regarded as an effectively closed quantum many-body system for a limited length ($< \ell_{\text{leak}}$), despite the fact that ohmic contacts and the measurement apparatus are attached. This would open the way to exploring many-body quantum dynamics in the solid states [36].

Appendix A: Device characteristics

1. Sample layout

We used two quantum Hall samples, Sample A for $L = 0.15$ and $0.5 \mu\text{m}$ and Sample B for $L = 5$ and $15 \mu\text{m}$, fabricated in standard modulation-doped AlGaAs/GaAs heterostructures.

For Sample A, the heterostructure shows electron density of $3.1 \times 10^{11} \text{ cm}^{-2}$ and low-temperature mobility of $1.9 \times 10^6 \text{ cm}^2/\text{Vs}$. A scanning electron micrograph (SEM) of a test sample is shown in Fig. S1(a), where surface metal gates with numbers 1 - 7 and the locations of ohmic contacts ($\Omega_1 - \Omega_4$ and crossed boxes) are shown. Edge channels C_\uparrow and C_\downarrow (not illustrated) were formed along the lower side of gate 1 and 2 with appropriate gate voltages under magnetic field $|B_{\text{exp}}| = 7.5 \text{ T}$. A quantum dot (QD) marked by the white circle was formed with gate 1, 2, 3, 4, and 5. Tunneling between C_\uparrow and QD was controlled with voltages on gate 1 and 2, and tunneling to the drain channel toward ohmic contact Ω_1 is tuned with the voltage on gate 5. For the measurement at $L = 0.12 \mu\text{m}$ [Fig. 2(a)], the injector QPC was formed with gate 6. The trace (i) in Fig. 2(a) was taken at positive B_{exp} with chirality from the QPC (gate 6) to the QD, while trace (i') was taken at negative B_{exp} under opposite chirality. The measurement at $L = 0.5 \mu\text{m}$ [Fig. 2(b)] was performed with the QPC formed by gate 7 (and 1) under negative B_{exp} with chirality from the QPC (7) to the QD.

For Sample B, the heterostructure shows electron density of $2.9 \times 10^{11} \text{ cm}^{-2}$ and low-temperature mobility of $1.6 \times 10^6 \text{ cm}^2/\text{Vs}$. An SEM of a test sample is shown in Fig. S1(b). Edge channels C_\uparrow and C_\downarrow (not illustrated) were formed along the upper side of the long gate 1 at $|B_{\text{exp}}| = 6 \text{ T}$. A QD spectrometer (white circle in the inset) was formed with gate 1, 5, 6, and 7, and a QPC injector is formed with gate 4 (and 1) for the measurement at $L = 5 \mu\text{m}$ under positive B_{exp} with chirality from the QPC(4) to the QD. All data in Fig. 3 was taken in this configuration. The measurement at $L = 5$ and $15 \mu\text{m}$ in Fig. 4(b) was performed with a QD spectrometer formed with gate 1, 2, 3, and 4, and various QPCs with gate 5, 7, 8, and 9 under negative B_{exp} with chirality from the QPCs to the QD. This configuration with QPC(gate 8) is schematically shown in Fig. 1(a).

2. QPC injector

Figure S2(a) shows the quantized conductance of QPC(gate 4) in Sample B which were used in the measurement of Fig. 3. The dimensionless conductance D was obtained from the total dc current I_S and the applied voltage V_S with the relation $V_S = I_S [(h/e^2)/D + R_{\text{ser}}]$. Here $R_{\text{ser}} \sim 1 \text{ k}\Omega$ is the series resistance including the ohmic resistances and the impedance of the measurement system. The voltage drop on R_{ser} is less than 10 % of V_S at $D = 2$ and negligibly small at $D \ll 1$. The conductance steps are clearly seen in Fig. S2(a) even at large bias voltage of $V_S = 400 \mu\text{V}$. As the conductance traces at $V_S = 100 \mu\text{V}$ and $200 \mu\text{V}$ are almost the same in the whole range $0 < D < 2$, the QPC is in a reasonably linear regime at $V_S \leq 200 \mu\text{V}$. The QD current profiles in Fig. 3(c) were taken under this condition. The nonlinear effect appears at higher bias as seen in the deformed trace

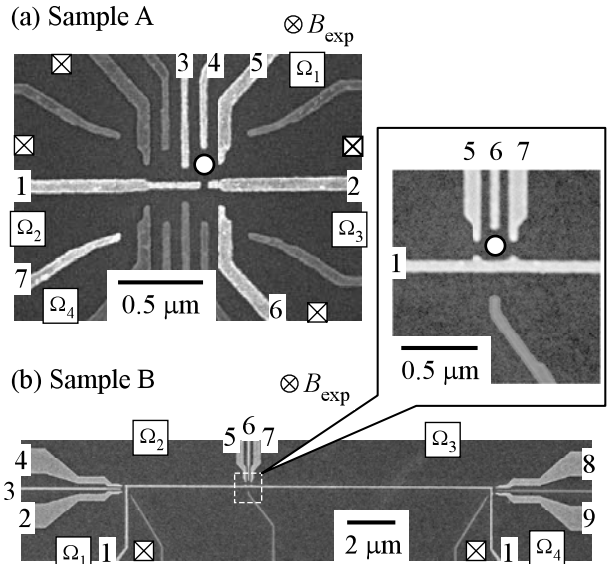


FIG. S1. (a) and (b) Scanning electron micrograph of Sample A in (a) and Sample B in (b). The surface of the GaAs heterostructure appears dark. Surface metal gates appear bright, but unused gates are darkened for better visibility.

at $V_S = 400 \mu\text{V}$ in Fig. S2(a). Figure S2(b) shows the I-V characteristics of the QPC at low $D < 0.1$. The data shows quite linear conductance up to $V_S = 500 \mu\text{V}$ for $D < 0.02$. The arctangent current profile in Fig. 3(a) was taken under this linear conductance profile. In this way, the nonlinearity of the QPC does not play a major role in the observation of non-Fermi distribution functions.

When the QPC enters the nonlinear region, the current increases rapidly with increasing V_S as shown in Fig. S2(b). As we evaluated $D \simeq (h/e^2) I_S/V_S$ from the average current I_S , the total heat and the thermalization temperature $T_{\text{th}} = \sqrt{\frac{3}{2}} \frac{1}{\pi k_B} \sqrt{D(1-D)} eV_S$ is underestimated in the nonlinear region. Moreover, the nonlinear effect can deflect the non-thermal state away from the theoretically predicted state. For quantitative analysis, we need further studies on the relation between electronic excitation with a nonlinear QPC and the distribution function of the non-thermal state.

3. QD characteristics

The QDs used in this work show the addition energy of 1 - 2 meV. The particular Coulomb blockade peak used to measure the data in Fig. 3 is shown in Fig. S3. The clear conductive region between the N - and $(N+1)$ -electron Coulomb blockade regions is seen with the onsets at $\varepsilon = \mu_D$ and $\varepsilon = \mu_\uparrow$. In addition to the transport through the ground state with ε , several current steps associated with excited states are seen. The features labeled ES (small steps at $V_D < 0$ and very faint steps marked by

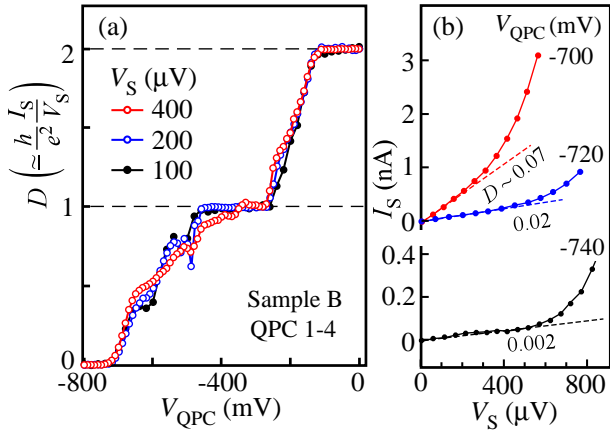


FIG. S 2. (a) The dimensionless QPC conductance D as a function of the gate voltage V_{QPC} . Nonlinearity of the QPC appears in some regions, such as $-650 \text{ mV} < V_{\text{QPC}} < -350 \text{ mV}$ at $V_S = 400 \mu\text{V}$. (b) Current (I_S) - voltage (V_S) characteristics of the QPC at several V_{QPC} for small D . The low-bias linear dependence is shown by dashed lines.

dots at $V_D > 0$) are associated with the first excited state of N -electron QD (the level spacing $\Delta \sim 350 \mu\text{eV}$). The features labeled ES' and ES'' are associated with the first and second excited states of $(N + 1)$ -electron QD (the level spacing $\Delta' \sim 250 \mu\text{eV}$ between the ground state and the first excited state). Extrapolating these excited-state features to the specific trace at $V_D = 200 \mu\text{V}$ (the red trace) are marked by downward triangles. All downward triangles shown in Fig. 1-4 were obtained in this way.

The current shows a peak at $\varepsilon = \mu_{\uparrow}$, which can be explained by the Fermi-edge singularity originated from the many-body effect between the localized state in the QD and electrons in C_{\uparrow} [37, 38]. While an arctangent current spectrum is suggested theoretically also for the Fermi-edge singularity, we did not observe such spectrum in our samples [the trace for $D = 0$ in Fig. 3(a)]. The Fermi-edge singularity should be significantly diminished by smearing the Fermi edge with increasing the temperature [37]. Therefore, we neglect the Fermi-edge singularity in the analysis of current tail for the non-thermal state.

For proving the distribution function f_{\uparrow} in C_{\uparrow} , it is desirable to have smaller incoming tunneling rate $\Gamma_{\uparrow}^{(G)}$ as compared to the outgoing tunneling rate $\Gamma_D^{(G)}$. We tuned the gate voltages such that $\Gamma_{\uparrow}^{(G)}/\Gamma_D^{(G)} \sim 0.1$ for the QD shown in Fig. S3. The asymmetric tunneling rates can be confirmed with the prominent excited-state features running parallel to the current onset at $\varepsilon = \mu_{\uparrow}$, as well as the Fermi-edge singularity seen at $\varepsilon = \mu_{\uparrow}$ but not at $\varepsilon = \mu_D$. We can deduce the tunneling rates from the saturated current by neglecting the Fermi-edge singularity. For the QD shown in Fig. S3, the tunneling rates across the left barrier to C_{\uparrow} are $\Gamma_{\uparrow}^{(G)} \simeq 100 \text{ MHz}$ for the ground

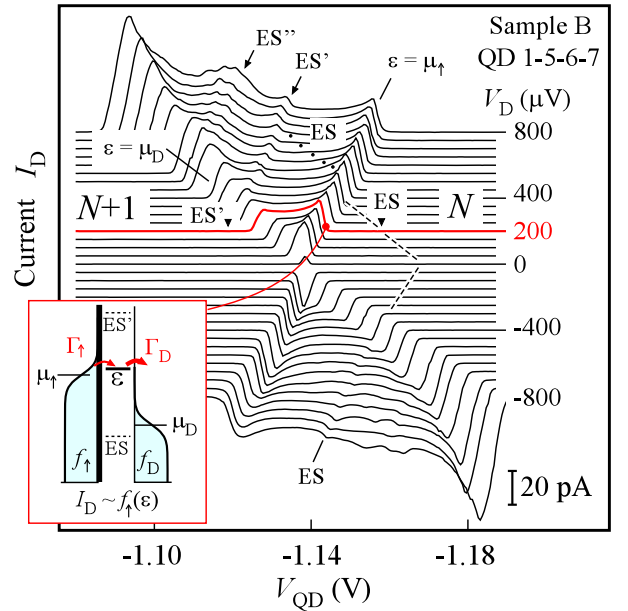


FIG. S 3. The QD current I_D as a function of the gate voltage V_{QD} for various bias voltage V_D , showing a Coulomb peak between N - and $(N + 1)$ -electron Coulomb blockade regions. Some excited-state features are marked. Each trace is offset for clarity. The inset shows the energy diagram of the transport.

state, $\Gamma_{\uparrow}^{(E)} \simeq 20 \text{ MHz}$ for ES, and $\Gamma_{\uparrow}^{(E')} \simeq 40 \text{ MHz}$ for ES'. As described below, small $\Gamma_{\uparrow}^{(E')} (< \Gamma_{\uparrow}^{(G)})$ is desirable for studying non-thermal states.

Appendix B: QD spectroscopy

Here, we characterize the QD spectroscopy particularly in the presence of excited states in the QD. The QD current is calculated by using rate equations for occupation probabilities in the QD states [35]. For simplicity, transport through the first excited state of N -electron QD, ES, and the first excited state of $(N + 1)$ -electron QD, ES', as well as the ground state are considered as shown in the energy diagram of Fig. S4(a). The corresponding tunneling rates $\Gamma_{\uparrow, D}^{(E)}$, $\Gamma_{\uparrow, D}^{(E')}$, and $\Gamma_{\uparrow, D}^{(G)}$ are considered to be independent of the QD states but asymmetric with respect to the left and right barriers; $\Gamma_{\uparrow}^{(E)} = \Gamma_{\uparrow}^{(E')} = \Gamma_{\uparrow}^{(G)} = 100 \text{ MHz}$ and $\Gamma_D^{(E)} = \Gamma_D^{(E')} = \Gamma_D^{(G)} = 1 \text{ GHz}$. Figure S4(b) shows the calculated Coulomb peak with energy spacing $\Delta = 350 \mu\text{eV}$ for ES and $\Delta' = 250 \mu\text{eV}$ for ES', where αV_{QD} is the electrostatic potential of the QD. Here, both edge channels C_{\uparrow} and C_D are considered to be in thermal equilibrium at the base temperature of 80 mK ($k_B T_{\uparrow} = k_B T_D = 6.8 \mu\text{eV}$). Some features associated with ES and ES' are indicated by arrows and dots, and their

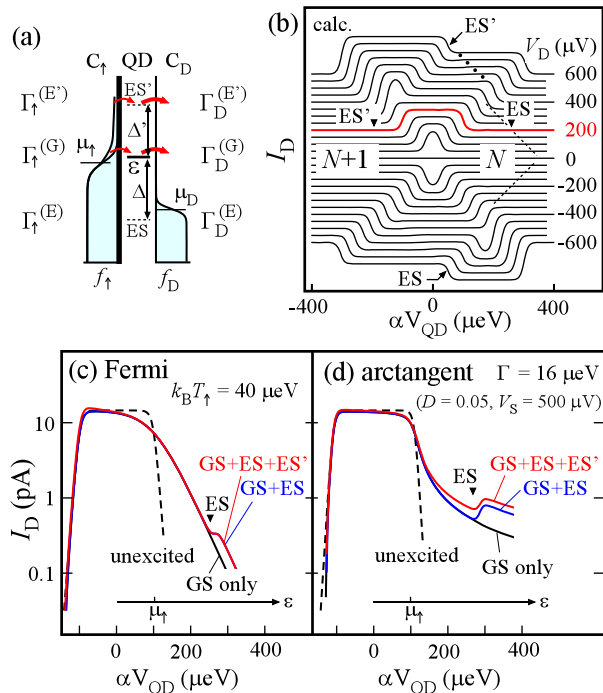


FIG. S 4. (a) Energy diagram of transport through a QD. ES and ES' are first excited states of N - and $(N+1)$ -electron QDs, respectively. (b) Calculated QD current I_D as a function of electrostatic potential αV_{QD} at various V_D . (c) and (d) I_D at $V_D = 200 \mu\text{V}$ with a heated Fermi distribution function for (c) and an arctangent function for (d) in C_{\uparrow} .

extrapolations to the $V_D = 200 \mu\text{V}$ trace are marked by downward triangles. The experimental features in Fig. S3 are well reproduced except for the step heights (not adjusted) and the Fermi edge singularity.

The QD current profile changes when C_{\uparrow} is excited. Solid lines in Fig. S4(c) and S4(d) show the QD current calculated when Fermi distribution function f_{FD} at $k_B T_{\uparrow} = 40 \mu\text{eV}$ in (c) and arctangent function f_{atn} (defined in the main part) with $\Gamma = 16 \mu\text{eV}$ in (d) are considered for C_{\uparrow} . $\Gamma = 16 \mu\text{eV}$ corresponds to the case at $D = 0.05$ and $V_S = 500 \mu\text{V}$. If there are no excited states in the QD, the current (the black solid line labeled 'GS only') is proportional to the distribution function $f_{\uparrow}(\epsilon)$ for $\alpha V_{QD} > 0$. If ES is included in the calculation, the current (the blue solid line labeled 'GS+ES') exhibits a stepwise increase at $\epsilon = \mu_D + \Delta$ (marked by the downward triangle). However, we did not observe clear signature of this current step in our measurements, probably because energy relaxation rate from ES to GS is larger than $\Gamma_{\uparrow}^{(E)}$ [35].

If ES', as well as ES and GS, are considered in the calculation, the QD current in Fig. S4(d) for the arctangent function is enhanced considerably at $\epsilon > \mu_{\uparrow}$ (the red solid line labeled "GS+ES+ES'"). In contrast, no significant change is seen in Fig. S4(c) with Fermi distribution function. The difference can be understood with the en-

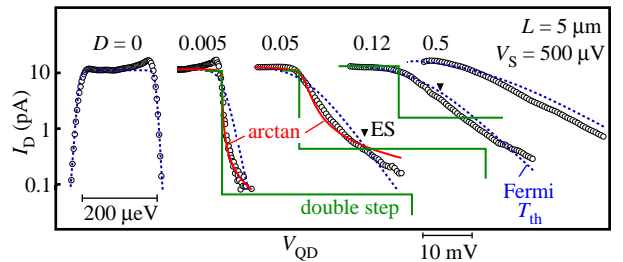


FIG. S 5. D dependence of the QD current at $V_S = 500 \mu\text{V}$ and $L = 5 \mu\text{m}$.

ergy diagram of Fig. 4(a), where the high-energy tail of the arctangent (Fermi) distribution function f_{\uparrow} gives non-negligible (negligible) current through ES'. The rate-equation solution gives $I_D \simeq \Gamma_{\uparrow}^{(G)} f_{\uparrow}(\epsilon) + \Gamma_{\uparrow}^{(E')} f_{\uparrow}(\epsilon + \Delta')$ for $\Gamma_{\uparrow} \ll \Gamma_D$ and $\alpha V_{QD} > 0$, which is independent of the energy relaxation rate from ES' to GS. The second term is negligible for Fermi distribution functions, but can contribute dominant current for the arctangent functions particularly when $\Gamma_{\uparrow}^{(E')}$ is greater than $\Gamma_{\uparrow}^{(G)}$. For the QD shown in Fig. S3, small contribution with $\Gamma_{\uparrow}^{(E')} \simeq 0.4\Gamma_{\uparrow}^{(G)}$ is expected. This explains why we see good agreement with the expected arctangent profile at $D = 0.005$ in Fig. 3(a). However, larger contribution is suggested with $\Gamma_L^{(E')} \simeq 10\Gamma_L^{(G)}$ and $\Gamma_L^{(E')} \simeq 2\Gamma_L^{(G)}$ for the QDs used to take the data shown in Fig. 4(a) and 4(b), respectively. This could be a reason for showing large current tail greater than the predicted arctangent form.

Appendix C: Non-thermal spectra

1. Transition between arctangent and Fermi functions

Figure S5 shows a D dependence of the QD current profile taken at $V_S = 500 \mu\text{V}$ ($\ell_{SC} = 0.22 \mu\text{m}$) and $L = 5 \mu\text{m}$. We find excellent agreement with the theoretically predicted arctangent function (red solid lines) $f_{atn}(E) = \frac{1}{2} - \arctan(E/\Gamma)/\pi$ at $D = 0.005$ with a single parameter $\Gamma = 2eDV_S/\pi$ that was determined from the measurement of I_S with $D \simeq (h/e^2)I_S/V_S$, and with the Fermi distribution function (blue dotted lines) for $T_{th} = \sqrt{\frac{3}{2}} \frac{1}{\pi k_B} \sqrt{D(1-D)}eV_S$ at $D = 0.5$. Smooth transition between them is clearly resolved at $0.005 < D < 0.5$.

2. D dependence

Here, we provide a detailed analysis of the D dependence of QD current profiles for $L = 5 \mu\text{m}$ presented in

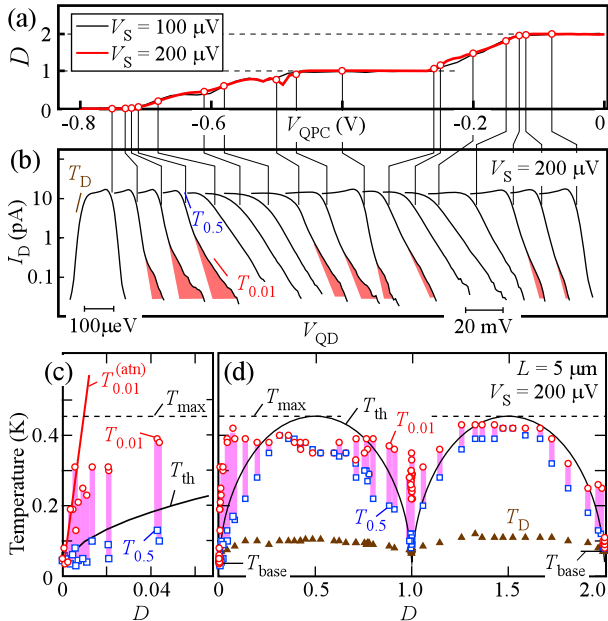


FIG. S 6. (a) Gate voltage V_{QPC} dependence of dimensionless conductance D . (b) The QD current spectra obtained at various V_{QPC} marked by circles in (a). Each trace is offset horizontally for clarity. Non-thermal distribution is highlighted by magenta regions. (c) and (d) D dependence of electron temperatures, $T_{0.5}$, $T_{0.01}$, and T_D obtained from the slopes depicted in (b), and $T_{0.01}^{(\text{atn})}$, T_{th} , and T_{max} from the model. A part of (c) is replotted in (b) with a magnified scale.

Figs. 3(b) and 3(c). For convenience, they are also shown in Figs. S6(a) and S6(b). The non-thermal distribution function can be characterized by non-exponential current rolloff. To clarify the region showing non-thermal distribution functions, we compare the slope of the rolloff at different f values. For convenience, we defined two temperatures, $T_{0.5}$ deduced from the data at $f \simeq 0.5$ [$k_{\text{B}}T_{0.5} = -\{2d(\ln f)/dE|_{f=0.5}\}^{-1}$], and $T_{0.01}$ at $f \simeq 0.01$ [$k_{\text{B}}T_{0.01} = -\{d(\ln f)/dE|_{f=0.01}\}^{-1}$]. The factor 2 difference in the definitions is introduced such that Fermi distribution functions always show $T_{0.5} = T_{0.01}$. As shown in Figs. S6(c) and S6(d), while nearly Fermi distribution function ($T_{0.5} \simeq T_{0.01}$) appears at frequent-tunneling conditions $D \simeq 0.5$ and $D \simeq 1.5$, non-Fermi distribution functions with a tail ($T_{0.5} < T_{0.01}$) are observed at sparse-tunneling conditions $0 < D < 0.3$, $0.7 < D < 1.3$, and $1.7 < D < 2$ (highlighted by vertical bars connecting circles for $T_{0.01}$ and squares for $T_{0.5}$). Qualitatively the same feature for both spin-up tunneling ($0 < D < 1$) and spin-down tunneling ($1 < D < 2$) is consistent with the energy exchange associated with the spin-charge separation.

The theoretically derived arctangent formula suggests that $T_{0.01}$ increases linearly with D , in a form $T_f^{(\text{atn})} = 2eV_S D / \pi^2 k_{\text{B}} f$ for small f ($= 0.01$ for the present case). Experimental plots of $T_{0.01}$ are scattered around $T_f^{(\text{atn})}$

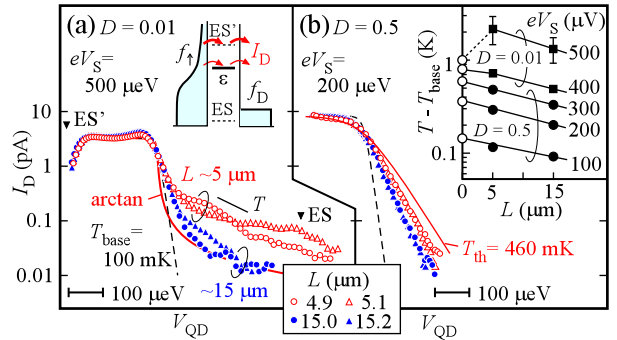


FIG. S 7. (a) and (b) QD current spectra showing non-thermal states at $L = 5$ and $15 \mu\text{m}$ for (a) $D = 0.01$ and (b) 0.5 . The inset to (b) shows the decay of the effective temperature T obtained from the slope of the tail.

only for small $D < 0.01$ (the solid line for $T_{0.01}^{(\text{atn})}$) in Fig. S6(c). However, $T_{0.01}$ does not follow $T_f^{(\text{atn})}$ at $D > 0.1$, and saturates at $D > 0.04$. It is almost constant over the wide range of D ($0.04 < D < 0.9$ and $1.2 \lesssim D \lesssim 1.8$) as seen in Fig. S6(d). While non-thermal states are seen in the wide range, the theoretically predicted arctangent form appear in the narrow range $D < 0.01$.

The constant slope ($T_{0.01}$) can be understood with the Fourier spectrum of the wavepackets. The frequency range of the packets is given by eV_S/h , while the excitation amplitude is proportional to $\eta = 4D(1 - D)$. If the excitation is characterized by the Fermi distribution function $f_{\text{FD}}(E; T_{\text{max}})$ with the maximum temperature T_{max} of T_{th} at $D = 0.5$ ($\eta = 1$) as suggested by the theory [8], the corresponding plasmon distribution follows the Bose distribution function $g_{\text{BE}}(\omega; T_{\text{max}})$ of plasmon frequency ω [5, 39]. When the excitation is reduced by the factor η (< 1), the plasmon distribution would also be reduced to $\eta g_{\text{BE}}(\omega; T_{\text{max}})$, and the corresponding electronic distribution can be written as $(1 - \eta)f_{\text{FD}}(E; T_{\text{base}}) + \eta f_{\text{FD}}(E; T_{\text{max}})$ by taking a crude approximation in the fermionization [28]. Since the second term dominantly determines $T_{0.01}$ at $0.01 < \eta \ll 1$, this explains the appearance of almost constant $T_{0.01}$ close to T_{max} [dashed lines in Figs. S6(c) and S6(d)] with the allowance of the heat leakage (about 20%) described below. This simple model does not work at $\eta < 0.01$, where the arctangent profile is well developed.

3. Heat leakage

The heat leakage is further investigated with the data shown in Fig. S7 for $L \simeq 5$ and $15 \mu\text{m}$. These data were measured using the same QD spectrometer while the excitation being done with different QPCs. For $D = 0.01$ in Fig. S7(a), the long tail of the distribution function is clearly seen at $L \simeq 15 \mu\text{m}$ as well as at $L \simeq 5 \mu\text{m}$. However, the current tail seems to be attenuated as L in-

creases from 5 to 15 μm , implying heat leakage to the environment. Since these QPCs enter the nonlinear regime at $V_S > 200 - 400 \mu\text{V}$, ambiguity in the injected heat is concerned. A similar signature of heat leakage is also seen in the QD current profiles in Fig. S7(b) taken at $D = 0.5$ and $V_S = 200 \mu\text{V}$ in the reasonably linear conductance region. We evaluated the effective temperature T from the slope of the tail in Figs. S7(a) and S7(b). As shown in the inset, $T - T_{\text{base}}$ (solid symbols), when plotted as a function of L , shows an exponential decay from $T_{\text{th}} - T_{\text{base}}$ (open circles) with no clear dependence on V_S and D . This decay length $\ell_{\text{leak}} \sim 20 \mu\text{m}$ is much longer than the spin-charge separation length ($\ell_{\text{SC}} = 0.2$

- 1 μm at $V_S = 500 - 100 \mu\text{V}$ by assuming $v_{\text{SC}} = 27 \text{ km/s}$), which manifests the long-lived metastable nature of the non-thermal state.

ACKNOWLEDGMENTS

We thank Yasuhiro Tokura and Keiji Saito for fruitful discussions. This work was supported by JSPS KAKENHI (JP26247051, JP15H05854), International Research Center for Nanoscience and Quantum Physics at Tokyo Institute of Technology, and Nanotechnology Platform Program of MEXT.

-
- [1] J. Gemmer, M. Michel, and G. Mahler, *Quantum Thermodynamics*, Lecture Notes in Physics 784, (Springer, Berlin Heidelberg, 2009).
- [2] B. L. Altshuler and A. G. Aronov, Electron-electron interaction in disordered conductors, *Electron-Electron Interactions in Disordered Systems* (ed. A. L. Efros and M. Pollak), p. 1, (North-Holland Physics Publishing, Amsterdam, Netherlands, 1985).
- [3] H. Pothier, S. Guéron, N. O. Birge, D. Esteve and M. H. Devoret, Phys. Rev. Lett. **79**, 3490 (1997).
- [4] T. Giamarchi, *Quantum Physics in One Dimension* (Oxford University Press, Oxford, England, 2004).
- [5] D. B. Gutman, Y. Gefen, and A. D. Mirlin, Phys. Rev. Lett. **101**, 126802 (2008).
- [6] A. Iucci and M. A. Cazalilla, Phys. Rev. A **80**, 063619 (2009).
- [7] A. Polkovnikov, K. Sengupta, A. Silva, and M. Vengalattore, Rev. Mod. Phys. **83**, 863 (2011).
- [8] I. P. Levkivskiy and E. V. Sukhorukov, Phys. Rev. B **85**, 075309 (2012).
- [9] T. Kinoshita, T. Wenger, D. S. Weiss, Nature **440**, 900 (2006).
- [10] M. Gring, M. Kuhnert, T. Langen, T. Kitagawa, B. Rauer, M. Schreitl, I. Mazets, D. A. Smith, E. Demler and J. Schmiedmayer, Science **337**, 1318 (2012).
- [11] Z. F. Ezawa, *Quantum Hall Effects: Field Theoretical Approach and Related Topics* (World Scientific Publishing, Singapore, 2008).
- [12] A. M. Chang, Rev. Mod. Phys. **75**, 1449 (2003).
- [13] E. Berg, Y. Oreg, E.-A. Kim, and F. von Oppen, Phys. Rev. Lett. **102**, 236402 (2009).
- [14] V. Freulon, A. Marguerite, J. M. Berroir, B. Plaças, A. Cavanna, Y. Jin and G. Fève, Nat. Commun. **6**, 6854 (2015).
- [15] M. Hashisaka, N. Hiyama, T. Akiho, K. Muraki and T. Fujisawa, Nature Physics **13**, 559 (2017).
- [16] E. Bocquillon, V. Freulon, J. M. Berroir, P. Degiovanni, B. Plaças, A. Cavanna, Y. Jin, and G. Fève, Nature Commun. **4**, 1839 (2013).
- [17] H. Inoue, A. Grivnin, N. Ofek, I. Neder, M. Heiblum, V. Umansky and D. Mahalu, Phys. Rev. Lett. **112**, 166801 (2014).
- [18] C. Altimiras, H. le Sueur, U. Gennser, A. Cavanna, D. Mailly, and F. Pierre, Nature Phys. **6**, 34 (2010).
- [19] H. le Sueur, C. Altimiras, U. Gennser, A. Cavanna, D. Mailly, and F. Pierre, Phys. Rev. Lett. **105**, 056803 (2010).
- [20] D. L. Kovrizhin and J. T. Chalker, Phys. Rev. Lett. **109**, 106403 (2012).
- [21] A. M. Lunde, S. E. Nigg, and M. Büttiker, Phys. Rev. B **81**, 041311 (2010).
- [22] M. G. Prokudina, S. Ludwig, V. Pellegrini, L. Sorba, G. Biasiol, and V. S. Khrapai, Phys. Rev. Lett. **112**, 216402 (2014).
- [23] N. Kumada, H. Kamata, and T. Fujisawa, Phys. Rev. B **84**, 045314 (2011).
- [24] v_{SC} is sensitive to v_S rather than v_C . The effect of the metallization on v_S is not understood well.
- [25] A. M. Lunde and S. E. Nigg, Phys. Rev. B **94**, 045409 (2016).
- [26] S. Komiyama, H. Hirai, M. Ohsawa, Y. Matsuda, S. Sasa and T. Fujii, Phys. Rev. B **45**, 11085 (1992).
- [27] G. Müller, D. Weiss, A. V. Khaetskii, K. von Klitzing, S. Koch, H. Nickel, W. Schlapp and R. Lösch, Phys. Rev. B **45**, 3932-3935 (1992).
- [28] K. Washio, R. Nakazawa, M. Hashisaka, K. Muraki, Y. Tokura, and T. Fujisawa, Phys. Rev. B **93**, 075304 (2016).
- [29] H. Kamata, N. Kumada, M. Hashisaka, K. Muraki, and T. Fujisawa, Nature Nano. **9**, 177 (2014).
- [30] M. Hashisaka, H. Kamata, N. Kumada, K. Washio, R. Murata, K. Muraki, and T. Fujisawa, Phys. Rev. B **88**, 235409 (2013).
- [31] N. Telang and S. Bandyopadhyay, Phys. Rev. B **48**, 18002 (1993).
- [32] M. G. Prokudina, V. S. Khrapai, S. Ludwig, J. P. Kotthaus, H. P. Tranitz and W. Wegscheider, Phys. Rev. B **82**, 201310 (2010).
- [33] E. Onac, F. Balestro, L. H. Willems van Beveren, U. Hartmann, Yu.V. Nazarov, and L. P. Kouwenhoven, Phys. Rev. Lett. **96**, 176601 (2006).
- [34] V. Venkatachalam, S. Hart, L. Pfeiffer, K. West, and A. Yacoby, Nat. Phys. **8**, 676 (2012).
- [35] T. Fujisawa, D. G. Austing, Y. Tokura, Y. Hirayama, S. Tarucha, J. Physics: Cond. Matt. (Topical Review) **15**, R1395 (2003).
- [36] A. Calzona, F. M. Gambetta, F. Cavaliere, M. Carrega and M. Sassetti, Phys. Rev. B **96**, 085423 (2017).

- [37] K. Tobias, C. Livio, R. Christian, W. Werner, G. Leonid, I. Thomas and E. Klaus, *New. J. Phys.* **19**, 023009 (2017).
- [38] A. S. Goremykina and E. V. Sukhorukov, *Phys. Rev. B* **95**, 155419 (2017).
- [39] J. von Delft and H. Schoeller, *Ann. Phys.* **7**, 225 (1998).